

A new quantum clock for measuring photoemission delay times

Daehyun You¹, Kiyoshi Ueda^{1,*}, Elena V. Gryzlova², Alexei N. Grum-Grzhimailo², Maria M. Popova³, Ekaterina I. Staroselskaya³, Oyunbileg Tugs⁴, Yuki Orimo⁴, Takeshi Sato^{4,5,6}, Kenichi L. Ishikawa^{4,5,6}, Paolo Antonio Carpeggiani⁷, Tamás Csizmadia⁸, Miklós Füle⁸, Giuseppe Sansone⁹, Praveen Kumar Maroju⁹, Alessandro D'Elia¹⁰, Tommaso Mazza¹¹, Michael Meyer¹¹, Carlo Callegari¹², Michele Di Fraia¹², Oksana Plekan¹², Robert Richter¹², Luca Giannessi^{12,13}, Enrico Allaria¹², Giovanni De Ninno^{12,14}, Mauro Trovò¹², Laura Badano¹², Bruno Diviacco¹², David Gauthier^{12,15}, Najmeh Mirian¹², Giuseppe Penco¹², Primož Rebernik Ribič¹², Simone Spampinati¹², Carlo Spezzani¹², Giulio Gaio¹², and Kevin C. Prince^{12,16,*}

¹ Institute of Multidisciplinary Research for Advanced Materials, Tohoku University, Sendai 980-8577, Japan

² Skobeltsyn Institute of Nuclear Physics, Lomonosov Moscow State University, Moscow 119991, Russia

³ Faculty of Physics, Lomonosov Moscow State University, Moscow 119991, Russia

⁴ Department of Nuclear Engineering and Management, Graduate School of Engineering, The University of Tokyo, 7-3-1 Hongo, Bunkyo-ku, Tokyo 113-8656, Japan

⁵ Photon Science Center, Graduate School of Engineering, The University of Tokyo, 7-3-1 Hongo, Bunkyo-ku, Tokyo 113-8656, Japan

⁶ Research Institute for Photon Science and Laser Technology, The University of Tokyo, 7-3-1 Hongo, Bunkyo-ku, Tokyo 113-0033, Japan

⁷ Institut für Photonik, Technische Universität Wien, 1040 Vienna, Austria

⁸ ELI-ALPS, ELI-HU Non-Profit Ltd., Dugonics tér 13, H-6720 Szeged, Hungary

⁹ Physikalisches Institut, Albert-Ludwigs-Universität Freiburg, 79106 Freiburg, Germany

¹⁰ University of Trieste, Department of Physics, 34127 Trieste, Italy

¹¹ European X-Ray Free Electron Laser Facility GmbH, Holzkoppel 4, 22869 Schenefeld, Germany

¹² Elettra-Sincrotrone Trieste, 34149 Basovizza, Trieste, Italy

¹³ ENEA C.R. Frascati, 00044 Frascati, Rome, Italy

¹⁴ Laboratory of Quantum Optics, University of Nova Gorica, Nova Gorica 5001, Slovenia

¹⁵ Now at LIDYL, CEA, CNRS, Université Paris-Saclay, CEA-Saclay, 91191 Gif-sur-Yvette, France.

¹⁶ Centre for Translational Atomaterials, Swinburne University of Technology, Melbourne, Australia

*Corresponding authors: kiyoshi.ueda@tohoku.ac.jp, prince@elettra.eu

The age of attosecond physics was ushered in by the invention of methods for probing phenomena on a time scale less than femtoseconds [1]. In photoemission, the Eisenbud-Wigner-Smith (EWS) time delay [2] is the interval between photon annihilation and emission of the electron, usually measured in attoseconds (10^{-18} seconds), and varies with the kinetic energy and the angle of emission of the electron wave packet. We present a new interferometric method of measurement, using two phase-locked Extreme Ultraviolet pulses of frequency ω and 2ω , from a Free-Electron Laser. Phase differences between one- and two-photon ionization channels are extracted, and used to derive the relative EWS delay for one- and two-photon ionization of neon as a function of emission angle. Agreement with theory is excellent. Competing techniques require the use of an IR field, which necessitates corrections, but our method is correction-free. This new quantum clock is a powerful tool for investigating ultrafast processes in atoms and molecules.

There is great theoretical and experimental interest in the investigation of photoemission delays [3, 4, 5, 6, 7, 8], and there are currently two methods for measuring them. In attosecond streaking [9], an ultrafast, short-wavelength pulse ionizes an electron, and a femtosecond infrared (IR) pulse acts as a streaking field, by changing the linear momentum of the electron. A related method is the attosecond clock technique [10, 11, 12, 13], in which circular polarization is used to measure tunneling ionization times.

The second main technique for measuring EWS delays is interferometric, and is known as RABBITT (Reconstruction of Attosecond Beating By Interference of Two-photon Transitions):

it uses a train of attosecond pulses dressed by a phase-locked IR pulse [14]. The pulse duration requirements are relaxed, for example, pulse trains and IR pulses of 30 fs duration may be used [6]. Usually the IR pulse is the fundamental of the odd harmonics in the pulse train, although Loriot *et al.* [15] reported a variant using the second harmonic. Recent work on phase retrieval includes a method based on photo-recombination [16], two-colour, two-photon ionization via a resonance [17], and a proposal to use successive harmonics of circularly polarized light [18].

Streaking, RABBITT and the last mentioned techniques depend on the extreme temporal precision with which an IR pulse can be synchronized with a short-wavelength pulse or pulse train, generated by conversion of part of the light from the same source as the IR. The IR field generally perturbs the results of all these methods, necessitating corrections during analysis, and use of a sufficiently low IR power. These corrections are termed the Coulomb-laser coupling shift for streaking, and continuum-continuum coupling shift for RABBITT [2]. To date, all such corrections have been made using theoretical calculations, and no measurements are available to test their accuracy.

Pazourek *et al.* [2] labelled streaking techniques “classical clocks”, as they depend only on classical fields, and interferometric methods “quantum clocks” as they depend on the wave nature of matter and light. With few exceptions [19], measurements are of relative time delays, for example emission from two different levels of the same atom [4], or from two different targets measured simultaneously [5] or sequentially [7].

The EWS delay depends on the photoelectron kinetic energy and may depend on its emission direction. There are two possible physical origins of anisotropy. When the outgoing electron moves in a potential which depends on direction, its time to leave the ion varies accordingly. Secondly, an electron wave packet may consist of two or more partial waves, with different angular momenta and phases. Since their angular distributions are different, these

partial waves interfere, introducing anisotropy. There has been significant theoretical work on the angle-dependent time delay, for example [20, 21, 22, 23, 24], but few related experimental reports [20, 25, 26], all using the RABBITT technique. The delay should be isotropic for one-photon ionization of He, but Heuser *et al.* [20] observed an angular dependence, attributed to the effect of the IR pulse, inherent in RABBITT interferometry.

The EWS delay is expressed as

$$\tau(E_k) = \frac{\partial \eta}{\partial E_k} \quad (1)$$

where τ is the angle-dependent electron wave packet group delay, η is the phase of the outgoing electron wave packet, and E_k is its kinetic energy, equal to the energy of the ionizing radiation minus the ionization potential of the target.

In the present work, we demonstrate measurements of the EWS delay that do not require an IR pulse. Using only fundamental and second harmonic wavelengths, we measure angular distributions of photoelectrons emitted from neon, and determine the phase relationships for one- and two-photon ionization. By analysing this data, we clock the angular dependence of the difference in EWS delay for electrons emitted by single- and two-photon processes. We use short-wavelength, phase-locked XUV (extreme ultraviolet) light. The extremely short pulses required for streaking are not needed, and instead extremely accurate phase control (few attoseconds) is exploited to access time resolution, as in other interferometric techniques. Suitable fine control is available from the Free-Electron Laser FERMI [27].

The beam consisting of the temporally overlapping harmonics irradiates a sample [28], shown schematically in Fig. 1. The intense fundamental radiation causes two-photon ionization, while the weak second harmonic gives rise to one-photon ionization. The energies of the photoelectrons created coherently in the two channels are identical, and electrons with the same linear momentum interfere [17]. The photoelectron angular distribution (PAD) is measured, and the wavelength is then changed and the measurement repeated. From the difference in phases

and electron energies at the two wavelengths, the derivative of the phase, Eq. (1), is calculated, yielding the EWS time delay.

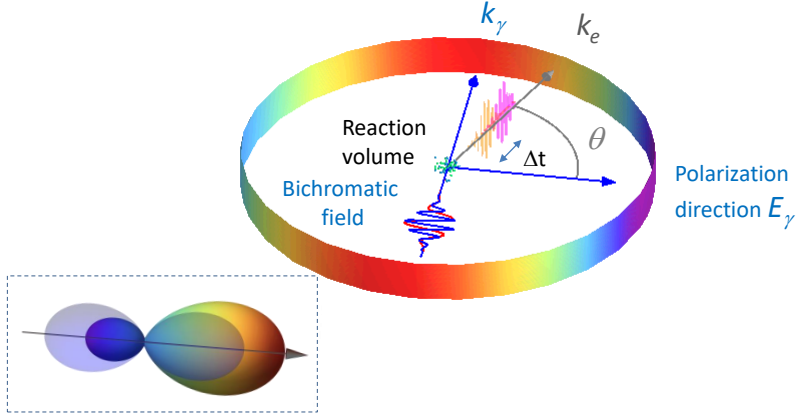


Fig. 1: Scheme of the experiment: bichromatic, linearly polarized light (red and blue waves), with momentum k_γ and electric vector E_γ , ionizes neon in the reaction volume. The electron wave packets (yellow and magenta waves) are emitted with electron momentum k_e . The time delay Δt between the amplitudes depends on emission angle; interference of two amplitudes leads to different electron signals for different angles. Inset, lower left: polar plot of photoelectron intensity at $E_k = 16.6$ eV for coherent harmonics (coloured) and incoherent harmonics (grey).

The sample consisted of a mixture of helium and neon, where the helium PAD was used to correct for phase offsets introduced when the photon energy was changed [29]. Further details are available in the Methods section.

The linearly polarized electric field is described by:

$$E(t) = \sqrt{I_\omega(t)} \cos \omega t + \sqrt{I_{2\omega}(t)} \cos(2\omega t - \phi). \quad (2)$$

where ω and 2ω are angular frequencies, $I_\omega(t)$ and $I_{2\omega}(t)$ are the pulse envelopes, ϕ denotes the

ω - 2ω relative phase.

We measured the PAD $I(\theta; \phi)$ at each optical phase ϕ , where θ is the polar angle from the polarization axis. The photoelectron intensity at a given angle oscillates as a function of the optical phase ϕ , see Figs. 2A and 2B:

$$I(\theta; \phi) = A_0(\theta) + A(\theta) \cos(\phi - \Delta\eta(\theta)), \quad (3)$$

where $\Delta\eta(\theta)$ is the difference between the phases for two-photon and one-photon ionization at each polar angle θ .

The theoretical descriptions of $I(\theta; \phi)$ and $\Delta\eta(\theta)$ are given in the Methods section. We extracted $\Delta\eta(\theta)$ from the measured PADs at three combinations of ω and 2ω (corresponding to photoelectron kinetic energies, 7.0 eV, 10.2 eV and 16.6 eV), at each polar angle. We assumed the symmetry $\Delta\eta(\theta) = \Delta\eta(\pi - \theta)$, as shown in Figs. 2A–2B. There is a significant increase of $\Delta\eta(\theta)$ at $\sim 90^\circ$, especially at 10.2 eV. The angular dependent variations of $\Delta\eta(\theta)$ at 7.0 eV and 16.6 eV are similar. We performed calculations for the phase shift differences $\Delta\eta(\theta)$ using both perturbation theory and real time *ab initio* methods (see Methods section) and both theories reproduce well the observed behaviour, see Figs. 2C– 2E.

Figure 3 shows the theoretical dependence of $\Delta\eta(\theta)$ on electron kinetic energy and polar angle θ . There is a single-photon $2p \rightarrow 3s$ resonance of the fundamental wavelength at 16.7 eV photon energy (12 eV kinetic energy.). The behaviour of $\Delta\eta$ in the region of the resonance is complicated: we can clearly see that $\Delta\eta(\theta)$ at $\theta \sim 90^\circ$ increases near the resonance around 12.0 eV and then returns to a value similar to that at ~ 7 eV. This clearly indicates that the large phase shift difference observed at 10.2 eV in Fig. 2D is due to the influence of the resonance at 12.0 eV [24, 25].

The variation of $\Delta\eta(\theta)$ below the resonance is smooth, so we can estimate the difference $\Delta\tau(\theta)$ in the EWS delay of two-photon ionization relative to one-photon ionization, employing

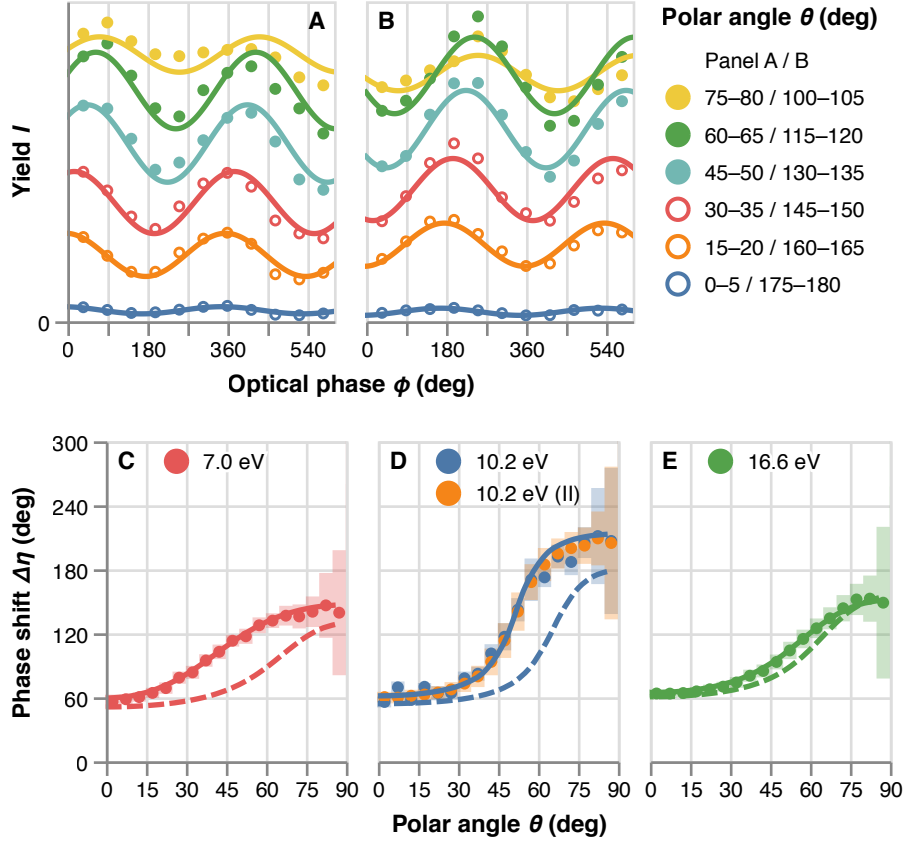


Fig. 2: Upper panels: typical photoelectron yields $I(\theta; \phi)$ as a function of optical phase ϕ at different polar angles θ . The signal was integrated over the 5° intervals shown on the right. The photoelectron kinetic energy is 7.0 eV. Circles are experimental results; lines are sinusoidal fits of the experimental results. Lower panels: extracted phase shift differences as a function of the polar angles, for four data sets and three photoelectron kinetic energies. Left (C): 7.0 eV; middle (D): 10.2 eV; right (E): 16.6 eV. Circles are experimental results; shaded areas show their uncertainties. Dashed lines: perturbation theory; solid lines: real time *ab initio* theory. Note that the curves in panels A and B oscillate in antiphase, because they correspond to emission directions on opposite sides of the photon propagation direction.

the energy points at 7.0 eV and 10.2 eV and assuming linear energy dependence. In Fig. 4, the experimental values of $\Delta\tau(\theta)$ at each polar angle θ are compared with the two theoretical values calculated from $\Delta\eta(\theta)$ at 7.0 eV and 10.2 eV. The observed delay difference is almost zero parallel to the polarization vector, but significant in the perpendicular direction; two-photon ionization is ~ 230 attoseconds slower than one-photon ionization at the average energy of

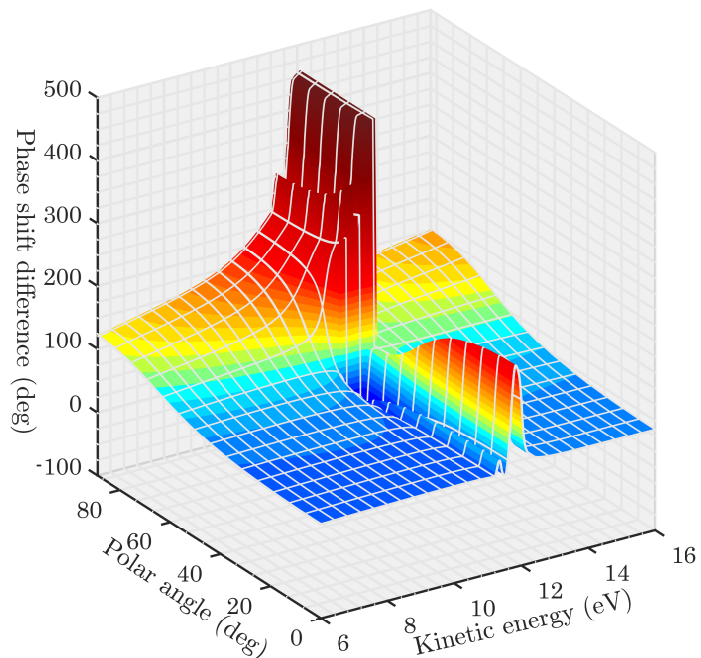


Fig. 3: Phase shift differences $\Delta\eta(\theta)$, calculated by perturbation theory, as a function of the polar angle θ and photoelectron kinetic energy. A large variation near 12.0 eV kinetic energy is due to the $2p \rightarrow 3s$ resonance.

8.6 eV. Both theories reproduce this behaviour well, with the time-dependent *ab initio* method exhibiting excellent agreement, validating the present experimental method.

The method is independent of the relative intensities of the fundamental and second harmonic radiation, see Eqs. (S14–S25), Methods section. This is a considerable experimental advantage, as it is not necessary to measure precisely the intensity and focal spot shape, and there are no effects due to volume averaging over the Gaussian spot profile.

The basic physics giving rise to the angular dependence of the EWS delay is clearly very complicated, and related to interference between wave packets emitted in one- and two-photon ionization, consisting of partial photoelectron waves with opposite parities. More details about the functional form of the angular dependence of the EWS delay is provided in the Methods

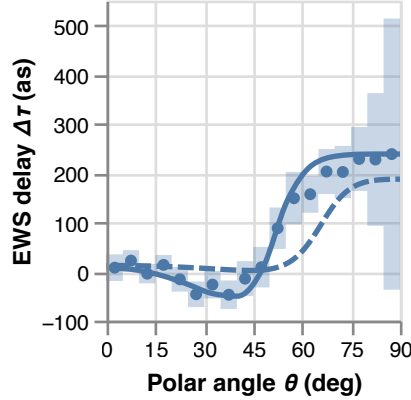


Fig. 4: EWS delay differences $\Delta\tau(\theta)$ of the two-photon ionization relative to the one-photon ionization. Theory and experiment, both estimated from two photoelectron energies 7.0 eV and 10.2 eV, are compared in the figure. Circles are experimental results; shaded areas show their uncertainties. Dashed line: result from perturbation theory; solid lines: result from the real time *ab initio* method.

section.

In this work we have described a new method to determine angle-resolved EWS time delay, and used it to measure the difference in delays between one- and two-photon ionization in Ne. Since the method is based on FEL radiation, it can be extended to shorter wavelengths, eventually to core levels, which lie in a wavelength region where optical lasers have reduced pulse energy. This is an important addition to the armoury of techniques available to attosecond science, gives access to the EWS delay for two-photon (even parity) transitions, and is applicable to molecules as well as atoms. It does not suffer from artifacts due to an IR pulse, which is necessary for angle-resolved RABBITT and streaking [30], and so is correction-free.

References

- [1] Krausz, F. & Ivanov, M. Attosecond physics. *Rev. Mod. Phys.* **81**, 163–234 (2009).
- [2] Pazourek, R., Nagele, S. & Burgdörfer, J. Attosecond chronoscopy of photoemission. *Rev. Mod. Phys.* **87**, 765–802 (2015).

- [3] Pabst, S. & Dahlström, J. M. Eliminating the dipole phase in attosecond pulse characterization using Rydberg wave packets. *Phys. Rev. A* **94**, 1–11 (2016).
- [4] Klünder, K. *et al.* Probing single-photon ionization on the attosecond time scale. *Phys. Rev. Lett.* **106**, 1–4 (2011).
- [5] Guénot, D. *et al.* Measurements of relative photoemission time delays in noble gas atoms. *J. Phys. B* **47**, 245602 (2014).
- [6] Guénot, D. *et al.* Photoemission-time-delay measurements and calculations close to the 3s-ionization-cross-section minimum in Ar. *Phys. Rev. A* **85**, 053424 (2012).
- [7] Palatchi, C. *et al.* Atomic delay in helium, neon, argon and krypton. *J. Phys. B* **47**, 245003 (2014).
- [8] Kheifets, A. S. Time delay in valence-shell photoionization of noble-gas atoms. *Phys. Rev. A* **87**, 063404 (2013).
- [9] Schultze, M. *et al.* Delay in photoemission. *Science* **328**, 1658–1662 (2010).
- [10] Eckle, P. *et al.* Attosecond Ionization and Tunneling Delay Time Measurements in Helium. *Science* **322**, 1525–1529 (2008).
- [11] Eckle, P. *et al.* Attosecond angular streaking. *Nat. Phys.* **4**, 565–570 (2008).
- [12] Pfeiffer, A. N. *et al.* Attoclock reveals natural coordinates of the laser-induced tunnelling current flow in atoms. *Nat. Phys.* **8**, 76–80 (2012).
- [13] Pfeiffer, A. N., Cirelli, C., Smolarski, M., Dörner, R. & Keller, U. Timing the release in sequential double ionization. *Nat. Phys.* **7**, 428–433 (2011).

- [14] Paul, P. M. *et al.* Observation of a train of attosecond pulses from high harmonic generation. *Science* **292**, 1689–1692 (2001).
- [15] Loriot, V. *et al.* Angularly resolved RABBITT using a second harmonic pulse. *J. Opt.* **19**, 114003 (2017).
- [16] Azoury, D. *et al.* Interferometric attosecond lock-in measurement of extreme-ultraviolet circular dichroism. *Nat. Photonics* **13**, 198–204 (2019).
- [17] Villeneuve, D. M., Hockett, P., Vrakking, M. J. J. & Niikura, H. Coherent imaging of an attosecond electron wave packet. *Science* **356**, 1150–1153 (2017).
- [18] Donsa, S., Douguet, N., Burgdörfer, J., Březinová, I. & Argenti, L. Circular holographic ionization-phase meter. *arXiv e-prints* arXiv:1904.04380 (2019).
- [19] Ossiander, M. *et al.* Absolute timing of the photoelectric effect. *Nature* **561**, 374377 (2018).
- [20] Heuser, S. *et al.* Angular dependence of photoemission time delay in helium. *Phys. Rev. A* **94**, 063409 (2016).
- [21] Mandal, A., Deshmukh, P. C., Kheifets, A. S., Dolmatov, V. K. & Manson, S. T. Angle-resolved Wigner time delay in atomic photoionization: The 4d subshell of free and confined Xe. *Phys. Rev. A* **96**, 1–9 (2017).
- [22] Ivanov, I. A. & Kheifets, A. S. Angle-dependent time delay in two-color XUV+IR photoemission of He and Ne. *Phys. Rev. A* **96**, 013408 (2017).
- [23] Bray, A. W., Naseem, F. & Kheifets, A. S. Photoionization of Xe and Xe and Xe@C₆₀ from the 4d shell in RABBITT fields. *Phys. Rev. A* **98**, 043427 (2018).

- [24] Banerjee, S., Deshmukh, P. C., Dolmatov, V. K., Manson, S. T. & Kheifets, A. S. Strong dependence of photoionization time delay on energy and angle in the neighborhood of Fano resonances. *Phys. Rev. A* **99**, 013416 (2019).
- [25] Cirelli, C. *et al.* Anisotropic photoemission time delays close to a Fano resonance. *Nat. Comm.* **9**, 955 (2018).
- [26] Vos, J. *et al.* Orientation-dependent stereo Wigner time delay and electron localization in a small molecule. *Science* **360**, 1326–1330 (2018).
- [27] Prince, K. C. *et al.* Coherent control with a short-wavelength free-electron laser. *Nat. Photonics* **10**, 176–179 (2016).
- [28] Shapiro, M. & Brumer, P. *Principles of the Quantum Control of Molecular Processes* (Wiley-Interscience, 2003).
- [29] M. Di Fraia *et al.*, submitted for publication.
- [30] Wei, H., Morishita, T. & Lin, C. D. Critical evaluation of attosecond time delays retrieved from photoelectron streaking measurements. *Phys. Rev. A* **93**, 053412 (2016).
- [31] Lyamayev, V. *et al.* A modular end-station for atomic, molecular, and cluster science at the low density matter beamline of FERMI@Elettra. *J. Phys. B* **46**, 164007 (2013).
- [32] Svetina, C. *et al.* The Low Density Matter (LDM) beamline at FERMI: optical layout and first commissioning. *J. Synchrotron Rad.* **22**, 538–543 (2015).
- [33] B. Diviacco, R. Bracco, D. Millo, M. Musardo, paper presented at IPAC'11, San Sebastian, Spain, September 2009.

- [34] Giannessi, L. *et al.* Coherent control schemes for the photoionization of neon and helium in the Extreme Ultraviolet spectral region. *Sci. Reports* **8**, 7774 (2018).
- [35] Zangrando, M. *et al.* Recent results of PADReS, the Photon Analysis Delivery and Reduction System, from the FERMI FEL commissioning and user operations. *J. Synchrotron Rad.* **22**, 565–570 (2015).
- [36] Raimondi, L. *et al.* Microfocusing of the FERMI@Elettra FEL beam with a KB active optics system: Spot size predictions by application of the WISE code. *Nucl. Instrum. Meth. A* **710**, 131–138 (2013).
- [37] Dribinski, V., Ossadtchi, A., Mandelshtam, V. A. & Reisler, H. Reconstruction of Abel-transformable images: The Gaussian basis-set expansion Abel transform method. *Rev. Sci. Instrum.* **73**, 2634–2642 (2002).
- [38] Amusia, M. Y. *Atomic Photoeffect* (New York, London: Plenum, 1990).
- [39] Varshalovich, D. A., Moskalev, A. N. & Khersonskii, V. K. *Quantum Theory Of Angular Momentum* (Singapore: World Scientific, 1988).
- [40] Dahlström, J. M. & Lindroth, E. Study of attosecond delays using perturbation diagrams and exterior complex scaling. *J. Phys. B* **47**, 124012 (2014).
- [41] Wätzel, J., Moskalenko, A. S., Pavlyukh, Y. & Berakdar, J. Angular resolved time delay in photoemission. *J. Phys. B* **48**, 025602 (2015).
- [42] Douguet, Nicolas, Gryzlova, Elena V., Staroselskaya, Ekaterina I., Bartschat, Klaus & Grum-Grzhimailo, Alexei N. Photoelectron angular distribution in two-pathway ionization of neon with femtosecond XUV pulses. *Eur. Phys. J. D* **71**, 105 (2017).

- [43] Orel, A. & Rescigno, T. An algebraic variational approach to the calculation of total cross sections for one- and two-photon ionization. *Chem. Phys. Lett.* **146**, 434–438 (1988).
- [44] Gao, B. & Starace, A. F. Variational principle for high-order perturbations with application to multiphoton processes for the H atom. *Phys. Rev. A* **39**, 4550–4560 (1989).
- [45] Staroselskaya, E. I. & Grum-Grzhimailo, A. N. A variationally stable method in the problem of two-photon atomic ionization. *Moscow Univ. Phys. Bull.* **70**, 374–381 (2015).
- [46] Gryzlova, E. V., Grum-Grzhimailo, A. N., Staroselskaya, E. I., Douguet, N. & Bartschat, K. Quantum coherent control of the photoelectron angular distribution in bichromatic-field ionization of atomic neon. *Phys. Rev. A* **97**, 013420 (2018).
- [47] Sato, T. & Ishikawa, K. L. Time-dependent complete-active-space self-consistent-field method for multielectron dynamics in intense laser fields. *Phys. Rev. A* **88**, 023402 (2013).
- [48] Sato, T. *et al.* Time-dependent complete-active-space self-consistent-field method for atoms: Application to high-order harmonic generation. *Phys. Rev. A* **94**, 023405 (2016).
- [49] Orimo, Y., Sato, T., Scrinzi, A. & Ishikawa, K. L. Implementation of the infinite-range exterior complex scaling to the time-dependent complete-active-space self-consistent-field method. *Phys. Rev. A* **97**, 023423 (2018).
- [50] Tao, L. & Scrinzi, A. Photo-electron momentum spectra from minimal volumes: the time-dependent surface flux method. *New J. Phys.* **14**, 013021 (2012).
- [51] Scrinzi, A. Infinite-range exterior complex scaling as a perfect absorber in time-dependent problems. *Phys. Rev. A* **81**, 053845 (2010).
- [52] Y. Orimo, T. Sato, K. L. Ishikawa, <https://arxiv.org/abs/1903.10743v2> (2019).

Acknowledgments

We thank the machine physicists of FERMI for making this experiment possible by their excellent work in providing high quality FEL light.

Funding. This work was supported in part by the X-ray Free Electron Laser Utilization Research Project and the X-ray Free Electron Laser Priority Strategy Program of the Ministry of Education, Culture, Sports, Science, and Technology of Japan (MEXT) and the IMRAM program of Tohoku University, and the Dynamic Alliance for Open Innovation Bridging Human, Environment and Materials program. DY wishes to thank supports by JSPS KAKENHI Grant Number JP19J12870, and a Grant-in-Aid of Tohoku University Institute for Promoting Graduate Degree Programs Division for Interdisciplinary Advanced Research and Education. EVG, EIS and MMP acknowledge the Foundation for the Advancement of Theoretical Physics and Mathematics “BASIS.” KLI gratefully acknowledges support by the Cooperative Research Program of the “Network Joint Research Center for Materials and Devices (Japan),” Grant-in-Aid for Scientific Research (Grants No. 16H03881, No. 17K05070, No. 18H03891, and No. 19H00869) from MEXT, the Photon Frontier Network Program of MEXT, the Center of Innovation Program from the Japan Science and Technology Agency, JST, CREST (Grant No. JPMJCR15N1), JST, Quantum Leap Flagship Program of MEXT, and Japan-Hungary Research Cooperative Program, JSPS and HAS. MM and TM acknowledge support by the Deutsche Forschungsgemeinschaft (DFG) under Grant No. SFB925/1. We acknowledge the support of the Italian Ministry of Research Project FIRB No. RBID08CRXK and No. PRIN 2010 ERFKXL 006, the bilateral project CNR JSPS Ultrafast science with extreme ultraviolet Free Electron Lasers, and funding from the European Union Horizon 2020 research and innovation program under the Marie Skłodowska-Curie Grant Agreement No. 641789 MEDEA (Molecular ElectronDynamics investigated by IntenseE Fields and Attosecond Pulses).

Author contributions. KU and KCP conceived and designed the experiment, wrote the proposal FERMI no. 20144077 which gained approval of the beamtime, and supervised the running of the experiment. CC, MDF, OP, DY, KU, PAC, TC, GS, PKM, ADE, KCP, MF, TM, MM, and RR participated in the experiment (operation of experimental station, acquisition of data, preliminary analysis, etc.), and LG, EA, GDN, MT, LB, BD, DG, NM, GP, PRR, SS, CS, GG participated in the experiment by operating the light source. KU and DY performed the detailed analysis of the experimental data. DY, KU, KLI, OT, YO, TS, EVG, MMP, EIS and ANGG analysed the theoretical description of the experiment and carried out calculations. KU and KCP drafted the manuscript, which was then reviewed and edited together with DY, KLI, ANGG and EVG, and circulated to all authors to obtain their input.

Competing interests. The Authors declare no competing interests.

Data and materials availability. All data needed to evaluate the conclusions in the paper are present in the paper or the Methods section. The code used to analyse the data is available at https://github.com/DaehyunPY/FERMI_20144077.

Methods

In the following sections, we give details of the experimental parameters and methods, the theoretical methods, and the data analysis.

Experimental Methods

The experimental methods have been described elsewhere [27] and are summarized here briefly. The experiment was carried out at the Low Density Matter Beamline [31, 32], using the Velocity Map Imaging spectrometer installed there. The relative phase of the two wavelengths was controlled by means of the electron delay line or phase shifter [33] used previously. It has been

calculated that the two pulses have good temporal overlap with slightly different durations and only a small mean variation of the phase within the Full Width at Half Maximum of the pulses, for example 0.07 rad for a fundamental photon energy of 18.5 eV (27).

The intensities of the two wavelengths for the experiments were set as follows. With the last undulator open (that is, inactive), the first harmonic from the first five undulators was set to a chosen wavelength. A small amount of incoherent second harmonic radiation (intensity of the order 1% of the fundamental) is produced by the undulators [34], and to absorb this, the gas filter available at FERMI was filled with helium. Helium is transparent at all of the fundamental wavelengths used in this study. The two-photon photoelectron signal from the neon and helium gas sample was observed with the VMI spectrometer. The last undulator was then closed to produce the second harmonic and the photoelectron spectrum of the combined beams was observed. The helium gas pressure in the gas cell was then adjusted to achieve a ratio of the ionization rates due to two-photon and one-photon ionization of 1:2 for kinetic energies of 7.0 and 10.2 eV. For the kinetic energy of 15.9 eV, the ratio was 1:4. The bichromatic beam was focused by adjusting the curvature of the Kirkpatrick-Baez active optics [35], and verified experimentally by measuring the focal spot size of the second harmonic with a Hartmann wavefront sensor. This instrument was not able to measure the spot size of the beams at the fundamental wavelengths, so it was calculated [36]. The measured spot was elliptical with a size $(4.5 \pm 1) \times (6.5 \pm 1) \mu\text{m}^2$ (FWHM), and the estimated pulse duration was 100 fs.

Tab. S1: Table of experimental parameters. E_k is the kinetic energy of the photoelectrons. Transmission takes account of reflection and geometric losses.

$\hbar\omega$, eV	E_k , eV	Pulse energy, μJ (exit undulator)	Transmission	Pulse energy, μJ (exp. station)	Average irradiance W/cm^2
14.3	7.0	45	0.16	7.2	3.6×10^{14}
15.9	10.2	95	0.20	19	1.0×10^{15}
19.1	16.6	84	0.29	24.4	1.2×10^{15}

The average pulse energies of the first harmonics at the exit of the undulators are given in Table S1, together with the kinetic energy of the electrons emitted via single-photon (2ω) or two-photon ($\omega + \omega$) ionization. The estimate of the pulse energy at 14.3 eV was indirect, since the gas cell monitors do not function at this energy, because they are based on ionization of nitrogen gas, and the photon energy is below the threshold for ionization. The approach was to first use the in-line spectrometer to measure spectra at 15.9 eV energy and simultaneously the pulse energies from the gas cell monitors, which gave a calibration of the spectrometer intensity versus pulse energy at this wavelength. Then spectrometer spectra were measured at 14.3 eV, and corrected for grating efficiency and detector sensitivity, to yield pulse energies. The pulse energies at the end-station were calculated by multiplying the values at the exit from the undulators by the transmission of the beamline [32]. Using the above spot sizes and pulse durations, the average irradiance at the sample was calculated, Table S1.

The atomic beam was produced by a supersonic expansion and defined by a skimmer and vertical slits. The length of the interaction volume along the light propagation direction was approximately 1 mm. The VMI data was analyzed using the BASEX method [37], which utilises an Abel transform to generate the Photoelectron Angular Distribution.

The sample consisted of a mixture of helium and neon. In other experiments [5, 7], use of two gases allowed referencing of the photoionization delay time of one electron to that of another. In the present case, we used the admixture of helium to resolve a technical problem: when the Free-Electron Laser wavelength is changed, the mechanical settings of the magnetic structures (undulators) creating the light are changed. This may introduce an unknown phase error between fundamental and second harmonic light. We have shown elsewhere that the PAD of helium $1s$ electrons can be used to determine the absolute phase, with input of only few theoretical parameters [29], and so helium was used as a reference.

Theoretical Methods: Angle-resolved wave packet time delay

We describe the electron wave packet at distance r sufficiently far away from the origin (the neon nucleus) as

$$\int_0^\infty c(\epsilon) e^{-i\epsilon t} e^{i(\sqrt{2\epsilon}r + \eta(\epsilon))} d\epsilon, \quad (\text{S1})$$

where ϵ is the photoelectron kinetic energy, $c(\epsilon)$ the real-valued amplitude, $\eta(\epsilon)$ the phase, and the dependence on direction $\{\theta, \varphi\}$ is implicit. We use Hartree atomic units unless otherwise stated. The group delay, interpreted as photoemission delay or time delay of this wave packet, is given by $\partial\eta(\epsilon)/\partial\epsilon$ (similar to the group delay of a laser pulse).

We consider here the wave packet created by the ω - 2ω electric field described by Equation (2) in the main text. In the ω - 2ω process, the wave packet is expressed as

$$\int_0^\infty e^{-i\epsilon t} e^{i\sqrt{2\epsilon}r} (c_\omega(\epsilon)e^{i\eta_\omega(\epsilon)} + c_{2\omega}(\epsilon)e^{i(\eta_{2\omega}(\epsilon)+\phi)}) d\epsilon. \quad (\text{S2})$$

The group delay of the one-photon and two-photon ionizations can be defined as $\partial\eta_\omega(\epsilon)/\partial\epsilon$ and $\partial\eta_{2\omega}(\epsilon)/\partial\epsilon$, respectively. The photoionization yield as a function of ϕ is given by

$$\begin{aligned} I(\phi) &= \int_0^\infty c_\omega(\epsilon)^2 + c_{2\omega}(\epsilon)^2 + 2c_\omega(\epsilon)c_{2\omega}(\epsilon) \cos(\phi - \Delta\eta(\epsilon)) d\epsilon \\ &\approx A_0 + A \cos(\phi - \Delta\eta(E_k)), \end{aligned} \quad (\text{S3})$$

where E_k is the average kinetic energy of the wave packet, and $\Delta\eta(\epsilon) \equiv \eta_\omega(\epsilon) - \eta_{2\omega}(\epsilon)$ is the phase of two-photon ionization relative to the one-photon ionization. Then,

$$\Delta\tau = \frac{\partial\Delta\eta(E_k)}{\partial E_k}, \quad (\text{S4})$$

can be considered as the delay difference between the two-photon and one-photon ionization wave packets.

This treatment may be generalized to the case of a few wave packets. In particular, expressing the photoionization yield as in Eq. (S3)

$$I(\phi) = A_0 + A \cos(\phi - \Delta\eta) = \sum_m A_{0,m} + A_m \cos(\phi - \Delta\eta_m), \quad (\text{S5})$$

where summation is over the wave packets. This leads to

$$A_0 = \sum_m A_{0,m}, \quad A \cos(\phi - \Delta\eta) = \sum_m A_m \cos(\phi - \Delta\eta_m). \quad (\text{S6})$$

The second equation can be viewed as the definition of the *average* $\Delta\eta$ of $\{\Delta\eta_m\}$.

Theoretical Methods: Perturbation theory

In the experiment, the number of optical cycles in the pulse is of the order of 400 for the fundamental and therefore we can treat the field as having constant amplitude and omit the initial phase of the field with respect to the envelope (carrier-envelope phase). Within the perturbation theory, we checked that our final results with an envelope including 100 optical cycles or more differ only within the optical linewidth from those obtained with the constant amplitude field. Thus, we describe the bichromatic electric field as

$$E(t) = F_0 (\cos \omega t + k \cos(2\omega t - \phi)) . \quad (\text{S7})$$

Furthermore, we make three assumptions: the dipole approximation for the interaction of the atom with the classically described electromagnetic field, the validity of the lowest nonvanishing order perturbation theory with respect to this interaction, and the LS-coupling approximation within the independent particle model for description of the atomic (ionic) structure. These approximations are well fulfilled for neon in the FEL spectral range and intensities of interest here. With these approximations, the photoelectron angular distribution $I(\theta, \varphi)$ of a Ne $2p$ electron can be derived by standard methods [38] in the form

$$I(\theta, \varphi) = I_0 \sum_{m=0,\pm 1} \left| \sum_{\xi} C_{\xi}^m(\phi) Y_{\ell\xi m}(\theta, \varphi) \right|^2, \quad (\text{S8})$$

where m is the magnetic quantum number of the initial $2p$ electron, $Y_{\ell m}(\theta, \varphi)$ is a spherical harmonic in the Condon-Shortley phase convention, I_0 is a normalization factor irrelevant to further discussion. The complex coefficients $C_\xi^m(\phi)$ depend on ionization amplitudes, and the index ξ denotes the ionization path. For one-photon ionization $\xi = \ell_\xi$, where ℓ_ξ is the orbital momentum of the photoelectron with possible values $\ell_\xi = s, d$. For two-photon ionization $\xi = \{\ell_\xi, \ell'_\xi\}$, where ℓ'_ξ is the orbital momentum of the virtual intermediate state, with possible combinations $\xi = ps, pd, fd$.

After applying the Wigner-Eckart theorem [39] to factor out the dependence on the projection m , the nonvanishing coefficients $C_\xi^m(\phi)$ may be expressed as (for brevity, we omit the argument ϕ when writing the coefficients):

$$C_s^0 = -\frac{1}{\sqrt{3}}D_s e^{i\phi}, \quad C_d^0 = \sqrt{\frac{2}{15}}D_d e^{i\phi}, \quad C_d^{\pm 1} = \frac{1}{\sqrt{10}}D_d e^{i\phi}, \quad (\text{S9})$$

$$\begin{aligned} C_{ps}^0 &= -\frac{1}{3}D_{ps}, & C_{pd}^0 &= -\frac{2}{15}D_{pd}, & C_{pd}^{\pm 1} &= -\frac{1}{10}D_{pd}, \\ C_{fd}^0 &= \frac{\sqrt{2}}{5\sqrt{7}}D_{fd}, & C_{fd}^{\pm 1} &= \frac{2}{5\sqrt{21}}D_{fd}. \end{aligned} \quad (\text{S10})$$

Here

$$D_\xi = d_\xi e^{i\eta_\xi} \quad (\text{S11})$$

are complex reduced matrix elements, independent of m with the absolute value

$$d_\xi = |D_\xi|. \quad (\text{S12})$$

and phase η_ξ . Note that one- (first order) and two-photon (second order) matrix elements (S11), both marked by a single index ξ , are proportional to the square root of intensity, and intensity of the field, respectively. Explicit expressions for D_ξ are presented below.

Equation (S8) can be readily cast into the form (S3), where

$$A_0(E_k) = \frac{I_0}{4\pi} \sum_{\lambda=\text{even}} Z_\lambda P_\lambda(\cos \theta), \quad A(E_k) = \frac{I_0}{4\pi} N, \quad (\text{S13})$$

$$\cos \Delta\eta(E_k) = N^{-1} \sum_{\lambda=\text{odd}} \text{Re} Z'_\lambda P_\lambda(\cos \theta), \quad (\text{S14})$$

$$\sin \Delta\eta(E_k) = N^{-1} \sum_{\lambda=\text{odd}} \text{Im} Z'_\lambda P_\lambda(\cos \theta), \quad (\text{S15})$$

$$N = \left| \sum_{\lambda=\text{odd}} Z'_\lambda P_\lambda(\cos \theta) \right|, \quad (\text{S16})$$

and

$$Z_\lambda = \sum_{m=0,\pm 1} \sum_{\xi\bar{\xi}} (-1)^m C_\xi^m C_{\bar{\xi}}^{m*} \sqrt{(2\ell_\xi + 1)(2\ell_{\bar{\xi}} + 1)} (\ell_\xi m, \ell_{\bar{\xi}} - m | \lambda 0) (\ell_\xi 0, \ell_{\bar{\xi}} 0 | \lambda 0), \quad (\text{S17})$$

where $(j_1 m_1, j_2 m_2 | j m)$ are Clebsch-Gordan coefficients [39]. The coefficients Z'_λ are expressed also by Eq. (S17), and with the values of C_ξ^m from Eqs. (S9), but omitting the factor $e^{i\phi}$. Equations (S9)–(S17) define $\Delta\eta(E_k)$, provided the reduced matrix elements (S11) are calculated. The intensities of the fundamental and of the second harmonic are factored out in the coefficients Z'_λ (see Eqs. (S22), (S25) below), therefore they cancel out in Eqs. (S14), (S15) and the phases $\Delta\eta(E_k)$ are independent of the intensities of the harmonics.

Note that the definition of the EWS delay $\Delta\eta(E_k)$ between one- and two-photon ionization implies not less than two ionization channels, which is reflected in the non-vanishing sum over channels in Eq. (S17). Therefore, the EWS delay is always angle-dependent in contrast to the case of pure one-photon ionization: the EWS delay for an isotropic initial state and isotropic residual ion is independent of the emission angle θ [40, 41]. For pure one-photon or pure two-photon ionization in which one channel has negligible amplitude, the EWS time delay may also be isotropic.

The coefficients (S17) are directly related to the anisotropy parameters β_λ in the angular

distribution of photoelectrons (S8) written in the form

$$I(\theta, \varphi) = \frac{W_0}{4\pi} \left(1 + \sum_{\lambda=1}^4 \beta_\lambda P_\lambda(\cos \theta) \right) \quad (\text{S18})$$

where

$$\beta_\lambda = \frac{Z_\lambda}{Z_0} \quad (\text{S19})$$

and $W_0 = I_0 Z_0$. Substituting Eqs. (S17) and (S9), (S10) into (S19) one can express the anisotropy coefficients in terms of complex reduced elements (S11). Examples of such expressions are given by Eqs. (7)–(11) of Ref. [42].

It immediately follows from Eqs. (S14), (S15)

$$\tan \Delta\eta = \frac{\text{Im}Z'_1 P_1(\cos \theta) + \text{Im}Z'_3 P_3(\cos \theta)}{\text{Re}Z'_1 P_1(\cos \theta) + \text{Re}Z'_3 P_3(\cos \theta)} = \frac{\text{Im}Z'_1 + f(\theta)\text{Im}Z'_3}{\text{Re}Z'_1 + f(\theta)\text{Re}Z'_3} \quad (\text{S20})$$

where the function $f(\theta) = \frac{1}{4}(5 \cos 2\theta - 1)$ is displayed in Fig. S1.

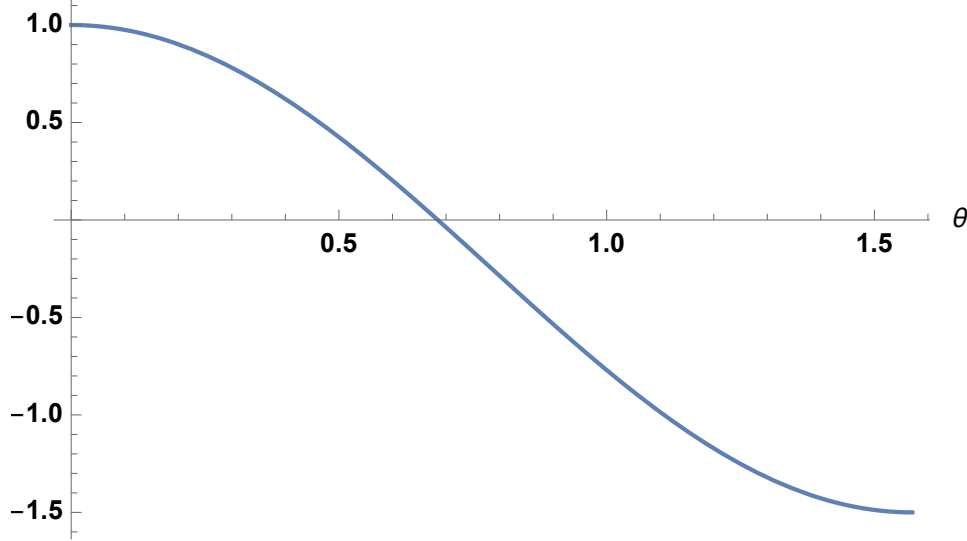


Fig. S1: Plot of $(5 \cos 2\theta - 1)/4$ as function of θ .

This qualitatively explains the quasi-cosine shape, and monotonic dependence of $\Delta\eta$ on θ (Fig. 2 C–E of the main text). Z'_λ are independent of ϕ , so that $\Delta\eta$ and the time delay are independent of the relative phase between the harmonics.

The functional form of Eq. (S20) is very general and valid, within the perturbation theory and the dipole approximation, for randomly oriented atoms and molecules, provided corresponding expressions for the coefficients Z_λ in terms of the ionization amplitudes are used. Moreover, it holds for circularly polarized collinear photon beams (except for chiral targets), provided the angle θ is measured from the direction of the beam propagation.

The reduced matrix element of the Ne one-photon $2p$ -ionization in first order perturbation theory can be cast in the conventional form [38]

$$D_\ell = i^{-\ell} e^{i\delta_\ell} A_\ell, \quad (\text{S21})$$

$$A_\ell = \sqrt{3}(10, 10 | \ell 0) \sqrt{I_{2\omega}} \int_0^\infty r^3 dr R_{E_k\ell}(r) R_{2p}(r), \quad (\text{S22})$$

where $R_{2p}(r)$ and $R_{E_k\ell}(r)$ are, respectively, the radial wave functions of the $2p$ electron and of the photoelectron with orbital momentum ℓ and energy E_k . The latter is real and possesses the asymptotic form

$$R_{E_k\ell}(r) = \frac{1}{\sqrt{\pi k}} \sin \left(kr - \frac{\ell\pi}{2} - \frac{1}{k} \ln 2kr + \delta_\ell \right), \quad (\text{S23})$$

δ_ℓ is the scattering phase, and $k = \sqrt{E_k} \text{ Ry}^{1/2}$. Furthermore, the second order reduced matrix element is of the form

$$D_{\ell\ell'} = i^{-\ell} e^{i\delta_\ell} A_{\ell,\ell'}, \quad (\text{S24})$$

$$A_{\ell,\ell'} = \sqrt{3(2\ell' + 1)}(10, 10 | \ell' 0)(\ell' 0, 10 | \ell 0) \times I_\omega \sum_n \int r'^3 dr' r^3 dr \frac{R_{E_k\ell}(r') R_{n\ell'}(r') R_{n\ell'}(r) R_{2p}(r)}{E_{2p} - E_n + \omega}, \quad (\text{S25})$$

where the summation/integration is over the unoccupied neon electronic states with energies E_n , radial wave functions $R_{n\ell'}$ and orbital momentum ℓ' . Note that A_ℓ and $A_{\ell,\ell'}$ both have dimensions of $[\text{Energy}]^{1/2}$. With our definitions in (S9)-(S11):

$$\eta_\ell = \begin{cases} \delta_\ell - \frac{\ell\pi}{2} & \text{for } A_\ell \geq 0, \\ \delta_\ell - \frac{\ell\pi}{2} + \pi & \text{for } A_\ell < 0 \end{cases}. \quad (\text{S26})$$

and similarly,

$$\eta_{\ell\ell'} = \begin{cases} \delta_\ell - \frac{\ell\pi}{2} & \text{for } A_{\ell\ell'} \geq 0, \\ \delta_\ell - \frac{\ell\pi}{2} + \pi & \text{for } A_{\ell\ell'} < 0 \end{cases}. \quad (\text{S27})$$

Our model for calculations of the first- and second-order ionization amplitudes in neon, the latter by the variationally stable method of infinite summation over the intermediate states in Eq. (S25) [43, 44, 45], was described and used recently in [46].

Fig. 2 in the main text depicts phase shift differences $\Delta\eta$ of two-photon ionization relative to one-photon ionization calculated by the recipe described above, as a function of the polar angle θ and photoelectron kinetic energy, while Fig. S2 depicts the corresponding EWS delay differences $\Delta\tau$ defined by Eq. (S4).

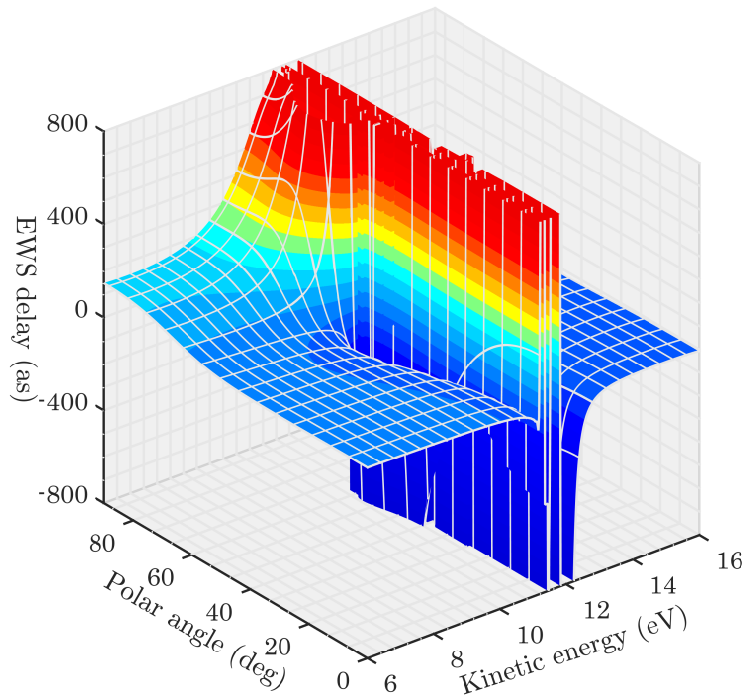


Fig. S2: Calculated EWS delay differences $\Delta\tau$ of two-photon ionization relative to one-photon ionization as a function of the polar angle θ and photoelectron kinetic energy below the $2p \rightarrow 3s$ resonance at 12.0 eV kinetic energy.

Theoretical Methods: Real-time *ab initio* simulations

We numerically simulated the photoionization of Ne irradiated by two-colour XUV pulses, using the time-dependent complete-active-space self-consistent field (TD-CASSCF) method [47, 48]. The dynamics of the laser-driven multielectron system is described by the time-dependent Schrödinger equation (TDSE),

$$i\frac{\partial\Psi(t)}{\partial t} = \hat{H}(t)\Psi(t), \quad (\text{S28})$$

where the time-dependent Hamiltonian is

$$\hat{H}(t) = \hat{H}_1(t) + \hat{H}_2, \quad (\text{S29})$$

with the one-electron part,

$$\hat{H}_1(t) = \sum_i \hat{h}(\mathbf{r}_i, t) \quad (\text{S30})$$

and the two-electron part,

$$\hat{H}_2 = \sum_{i=1}^N \sum_{j<i} \frac{1}{|\mathbf{r}_i - \mathbf{r}_j|}. \quad (\text{S31})$$

We employ the velocity gauge for the laser-electron interaction in the one-body Hamiltonian:

$$\hat{h}(\mathbf{r}, t) = \frac{\hat{\mathbf{p}}^2}{2} + \mathbf{A}(t) \cdot \hat{\mathbf{p}} - \frac{Z}{|\mathbf{r}|}, \quad (\text{S32})$$

where $\mathbf{A}(t) = -\int \mathbf{E}(t)dt$ is the vector potential, and $\mathbf{E}(t)$ is the laser electric field, see Eq. (2) in the main text, and Z ($=10$ for Ne) the atomic number.

In the TD-CASSCF method, the total electronic wave function is given in the configuration interaction (CI) expansion,

$$\Psi(\vec{x}_1, \vec{x}_2, \dots, \vec{x}_N, t) = \sum_I C_I(t) \Phi_I(\vec{x}_1, \vec{x}_2, \dots, \vec{x}_N, t). \quad (\text{S33})$$

where \vec{x} is a set of a spin coordinates σ and spatial coordinates \vec{r} . The electronic configuration $\Phi_I(\vec{x}_1, \vec{x}_2, \dots, \vec{x}_N, t)$ is a Slater determinant composed of spin orbital functions $\{\psi_p(\vec{r}, t) \times$

$s(\sigma)$, where $\{\psi_p(\vec{r}, t)\}$ and $\{s(\sigma)\}$ denote spatial orbitals and spin functions, respectively. Both the CI coefficients $\{C_I\}$ and orbitals vary in time.

The TD-CASSCF method classifies the spatial orbitals into three groups: doubly occupied and time-independent frozen core (FC), doubly occupied and time-dependent dynamical core (DC), and fully correlated active orbitals:

$$\Psi = \hat{A} \left[\Phi_{\text{fc}} \Phi_{\text{dc}} \sum_I \Phi_I C_I \right], \quad (\text{S34})$$

where \hat{A} denotes the antisymmetrization operator, Φ_{fc} and Φ_{dc} the closed-shell determinants formed with numbers n_{fc} FC orbitals and n_{dc} DC orbitals, respectively, and $\{\Phi_I\}$ the determinants constructed from n_a active orbitals. We consider all the possible distributions of active electrons among active orbitals. Thanks to this decomposition, we can significantly reduce the computational cost without sacrificing the accuracy in the description of correlated multi-electron dynamics. The equations of motion that describe the temporal evolution of the CI coefficients $\{C_I\}$ and the orbital functions $\{\psi_p\}$ are derived by use of the time-dependent variational principle [47]. The numerical implementation of the TD-CASSCF method for atoms is detailed in Refs. [48, 49].

Extraction of the photoelectron angular distribution and the phase shift difference

From the obtained time-dependent wave functions, we extract the angle-resolved photoelectron energy spectrum (ARPES) by use of the time-dependent surface flux (tSURFF) method [50]. This method computes the ARPES from the electron flux through a surface located at a certain radius R_s , beyond which the outgoing flux is absorbed by the infinite-range exterior complex scaling [51, 49].

We introduce the time-dependent momentum amplitude $a_p(\mathbf{k}, t)$ of orbital p for photoelec-

tron momentum \mathbf{k} , defined by,

$$a_p(\mathbf{k}, t) = \langle \chi_{\mathbf{k}}(\mathbf{r}, t) | u(R_s) | \psi_p(\mathbf{r}, t) \rangle \equiv \int_{r > R_s} \chi_{\mathbf{k}}^*(\mathbf{r}, t) \psi_p(\mathbf{r}, t) d^3 \mathbf{r}, \quad (\text{S35})$$

where $\chi_{\mathbf{k}}(\mathbf{r}, t)$ denotes the Volkov wavefunction, and $u(R_s)$ the Heaviside function which is unity for $r > R_s$ and vanishes otherwise. The use of the Volkov wavefunction implies that we neglect the effects of the Coulomb force from the nucleus and the other electrons on the photoelectron dynamics outside R_s , which has been confirmed to be a good approximation [52]. The photoelectron momentum distribution $\rho(\mathbf{k})$ is given by,

$$\rho(\mathbf{k}) = \sum_{pq} a_p(\mathbf{k}, \infty) a_q^*(\mathbf{k}, \infty) \langle \Psi(t) | \hat{E}_p^q | \Psi(t) \rangle, \quad (\text{S36})$$

with $\hat{E}_p^q \equiv \sum_{\sigma} \hat{a}_{q\sigma}^\dagger \hat{a}_{p\sigma}$. One obtains $a_p(\mathbf{k}, \infty)$ by numerically integrating,

$$-i \frac{\partial}{\partial t} a_p(\mathbf{k}, t) = \langle \chi_{\mathbf{k}}(t) | [h_s, \theta(R_s)] | \psi_p(t) \rangle + \sum_q a_q(\mathbf{k}, t) \{ \langle \psi_q(t) | \hat{F} | \psi_p(t) \rangle - R_p^q \}, \quad (\text{S37})$$

where $R_p^q = \langle \psi_q | \dot{\psi}_p \rangle - \langle \psi_q | \hat{h} | \psi_p \rangle$, and \hat{F} denotes a nonlocal operator describing the contribution from the inter-electronic Coulomb interaction [48, 49]. The numerical implementation of tSURFF to TD-CASSCF is detailed in Ref. [52].

We evaluate the photoelectron angular distribution $I(\theta)$ as a slice of $\rho(\mathbf{k})$ at the value of $|\mathbf{k}|$ corresponding to the photoelectron peak, and as a function of the optical phase ϕ . Then, employing a fitting procedure very similar to that used for the experimental data, we extract the phase shift difference $\Delta\eta$ between one-photon and two-photon ionization at photoelectron energies 7.0 eV, 10.2 eV and 16.6 eV. The results are shown in Fig. 2 in the main text.